ELSEVIER

Contents lists available at ScienceDirect

Additive Manufacturing

journal homepage: www.elsevier.com/locate/addma

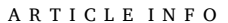


Research Paper

Modeling the selective laser melting-based additive manufacturing of thermoelectric powders

Yongjia Wu^{a,b}, Kan Sun^b, Shifeng Yu^b, Lei Zuo^{b,*}

- ^a School of Civil Engineering and Architecture, Wuhan University of Technology, Wuhan 430070, China
- ^b Department of Mechanical Engineering, Virginia Tech, Blacksburg, VA 24060, USA



Keywords:
Powder bed fusion
Selective laser melting
Thermoelectric
Numerical simulation
Material processing

ABSTRACT

Thermoelectric generators directly convert thermal energy to electricity when exposed to the proper temperature difference. The efficiency of the thermoelectric module has not been fully explored due to the drawbacks in conventional design and fabrication methods. Selective laser melting (SLM) additive manufacturing offers a unique potential scalable approach for the fabrication of flexible and functionally graded thermoelectric materials with high energy conversion efficiency. In this paper, we developed a physical model to simulate the SLM manufacturing process of thermoelectric materials (Mg₂Si powders) with additive material (Si) mixed for better thermoelectric performance. A comprehensive thermal and fluid study of the SLM manufacturing was conducted to understand the phenomena associated with the melting and solidification processes in the melting pool. This physical model was established based on the conservation equations and provided a basis to study the fluid flow driven by the buoyancy force and surface tension in the melting pool. Using this model, the influences of the process parameters, such as laser scanning speed and power energy density, on the temperature distribution, powder bed shrinkage, pool size, and particle aggregation in the powder bed, were studied, which provided critical information for understanding SLM for thermoelectric device fabrication.

1. Introduction

Thermoelectric generators can directly convert thermal energy to electrical energy using electrons and holes as a "working fluid" [1]. The conventional methods for fabricating thermoelectric materials, such as hot press and spark plasma sintering, are not perfect for large-volume thermoelectric module fabrication because of the drawbacks in practice, such as the long processing time and assembly process. Selective laser melting (SLM, Fig. 1), on the other hand, has been considered as an emerging technology for thermoelectric material fabrication because of its ability to fabricate components with any arbitrary shape. During the SLM, the chemical composition of powders can be adjusted by modifying the amount of additive, which makes it possible to implement functional doping along the thermo-element. This allows for the conversion efficiency of the thermoelectric module to be improved.

SLM fabrication is a laser-aided (Fig. 1(a)) powder bed fusion process in which a high-power laser is employed to fuse specific powders into a solid part with desired physical properties. Kruth et al. [2] described the details of the working principle of the SLM. SLM can fabricate components with a resolution as high as $10-200 \ \mu m$. Due to its high energy

density, SLM is particularly suitable for the fabrication of high melting point materials with high density without adhesives for binding purposes. This characteristic makes it ideal for the fabrication of thermoelectric materials.

During SLM fabrication of thermoelectric materials, the powders change from solid phase to liquid phase and then back to solid phase rapidly (Fig. 1(b)). A moving liquid-solid boundary is created by the moving laser. Though an inert gas environment is maintained during the SLM fabrication, oxidation can occur even if a small amount of oxygen exists in the environment. With operating temperatures as high as 1500 °C, severe evaporation can have negative impacts on the physical properties of the deposited materials. At the edge of the melting pool, the powders are in a state of partial solid and liquid making its properties different from the rest of the powder bed. The physical properties of the final products highly depend on the temperature evolution and temperature residence time. Changing the SLM process parameters, such as the powder characteristics, the chemical composition of powders, the laser wavelength, power, scan speed, and spacing, dramatically influence the physical properties of the resulting part - such as density, surface quality, and microstructures,

Wu et al. [3] proposed a novel optimization method for the

^{*} Corresponding author.

E-mail address: leizuo@vt.edu (L. Zuo).

Nomen	clature	K_0	permeability coefficient		
		β_T	thermal expansion coefficient, K^{-1}		
Symbols		eta_s	solute expansion coefficient, K^{-1}		
u_b	laser beaming moving speed, m/s	T_e	eutectic temperature, K		
u, v, w	velocities in x , y , and z directions, m/s	T_{M}	melting point temperature, K		
x, y, z	coordinates, m	k	equilibrium partition ratio		
W_{S}	velocity caused by powder shrinkage, m/s	T_a	ambient temperature, K		
p	pressure, Pa	θ	energy absorption coefficient		
μ^+	effective viscosity, $kg/(m \cdot s)$	$arepsilon_b$	emissivity		
T	temperature, K	h_c	convective heat transfer coefficient, $W/(m^2 \cdot K)$		
t	time, s	R	laser diameter, m		
g	gravity acceleration, m/s^2	σ_b	Boltzmann constant		
k^+	effective thermal conductivity, $W/(m \cdot K)$	$\partial\sigma/\partial T$	change rate of surface tension, $N/(m \cdot K)$		
S_h	energy source term, W/m^3	q_0	laser intensity, W/m^2		
S_C	nano-particle concentration source term, m^{-3}	v_s, v_n	velocity parallel and perpendicular to the surface, m/s		
D^{+}	effective diffusive coefficient, m^2/s	σ_{s}	surface tension, N/m		
C^+	effective concentration ratio	Ψ	limiter function		
ε	porosity	a_E, a_W, a_W	$a_E, a_W, a_N, a_S, a_F, a_B, a_P$ TVD coefficients		
s	shrinkage, m	D_e , D_v	$_{v}, D_{n}, D_{s}, D_{f}, D_{b}$ diffusion conductance, $kg/(m^{2} \cdot s)$		
T_{M}	melting temperature, K		F_n, F_s, F_f, F_b convective mass flux, $kg/(m^2 \cdot s)$		
ΔT	temperature difference, K	φ	variable to be solved		
H, h	enthalpy, J/kg	S_u^{DC}	the deferred correction source term		
f_s, f_l	solid and liquid mass faction	r	ratio of gradients		
k_s, k_l	solid and liquid thermal conductivity, $W/(m \cdot K)$,	rado or gradiento		
k_p, k_g	powder and gas thermal conductivity, $W/(m \cdot K)$	Abbrevi	iations		
C_s	nano-particle concentration ratio in solid and liquid	SLM	selective laser melting		
φ	the concentration radio	TEG	thermoelectric generator		
c_p	specific heat, $J/(K \cdot kg)$	CFD	computational fluid dynamics		
ρ	density, kg/m ³	AMC	Aluminum matrix composites		
μ_1	liquid viscosity, $kg/(m \cdot s)$	FVM	finite volume method		
μ_s	solid viscosity, $kg/(m \cdot s)$	TVD	total variation diminishing		
D	specific diffusion coefficient, m^2/s	ADI	alternating direction implicit		
_ L	latent heat, J/kg	BCM	block correction method		

construction of high-efficiency segmented TEGs in recent literature. The cross-sectional area of the thermoelectric element varied with the temperature profile to optimize for high energy conversion efficiency. This complicated geometry could only be practically realized by SLM. Nanoengineering offered unparalleled opportunities for manipulating the transport of electrons and phonons to improve the figure-of-merit (ZT) of thermoelectric materials [4–7]. During SLM, the grain boundaries of the nanocomposites can be well preserved by manipulating the laser power or process. In the recent years, many researchers began to explore the potential using SLM for thermoelectric material manufacturing. Thimont and LeBlanc [8] pointed out that it was feasible to fabricate thermoelectric generator (TEG) with novel leg geometry with the advance of additive manufacturing. They simulated the thermoelectric performance of TEGs with various leg geometries, such as prismatic, hollow, and layered structures. El-Desouky et al. [9] did a preliminary

experiment to examine the possibility to rapid processing the thermoelectric materials, for example Bi_2Te_3 . They [10] observed the microstructure of the thermoelectric materials fabricated by the SLM method. The results showed that SLM could potentially provide an attractive alternative way for the fabrication of thermoelectric materials. Carter et al. [11] investigated nanosecond pulsed laser melting of Bi_2Te_3 . A simplified model was established to simulate the heating phenomenon during the nanosecond pulsed laser melting process. Kang et al. [12] described a novel approach to fabricate functionally graded silicon matrix composites by the SLM method. During the fabrication, the material ingredient could be manipulated so that composite could achieve the best overall performance. Mingo et al. [4] presented a "nanoparticle-in-alloy" material approach to fabricated SiGe alloys, another thermoelectric material. The nanoparticle size was optimized to reduce the thermal conductivity of the alloy, resulting in a 5-fold increase in the ZT

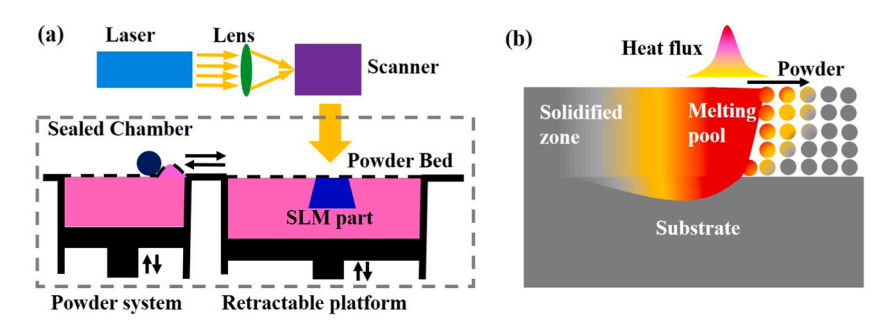


Fig. 1. (a) The working principle of SLM; and (b) SLM fabrication of powders.

value of the SiGe alloys at room temperature and 2.5 times increase at 900 K. Wang et al. [5] described a doping method to modulate the electronic band structure and/or minority carrier scatterings preference to reduce the bipolar thermal conductivity. Mao et al. [13] recently demonstrated an averaged ZT of ~0.7 in the temperature between 300 and 550 K in n-type Bi₂Te_{2.7}Se_{0.3} fabricated by laser melting. The performances of the fabricated thermoelectric materials were comparable to commercially-available materials. In their work, they also did a series of tests to find the best processing parameters for the fabrication of thermoelectric materials. Yan et al. [14] reported a nonequilibrium fabrication method of n-type CoSb_{2.85}Te_{0.15} using SLM. The influence of the processing parameters, such as the laser power and scanning speed, on the quality of the deposited layers was analyzed, and the optimal processing window for SLM was identified. Wu et al. [15] developed a fabrication method combined non-contact dispenser printing with selective laser melting (SLM) to process n-type Bi₂Te₃-based materials. However, there were few adequate models to analyze the impacts of the processing parameters on the deposited thermoelectric materials.

Fluid behavior has a significant influence on the physical properties of the printed materials. The flow pattern associated with the heat and mass transfer processes within the melting pool strongly depends on the fluid phenomenon, such as viscosity, thermo-capillary, surface tension, wetting, oxidation, and evaporation. Therefore, there is a need to establish a sound and comprehensive physical model which can be utilized to study the impacts of the process parameters on the sintered materials. Computational heat and mass transfer modeling [16,17] and the lattice Boltzmann simulation [18,19] are two important tools to address this issue. Computational heat and mass transfer method has been a common tool for the modeling of the melting and re-solidification process. SLM fabrication shares many characteristics with welding. The physical model of SLM can be adapted from the models summarized by Voller and Brent [20] for the modeling of binary alloy solidification systems existing in the welding process. The authors classified the models into three general one-phase models according to the problem domain. And the case study found that these models successfully predicted the aggregation patterns during the solidification. Li et al. [17] established a three-dimensional numerical model to study the laser melting of ceramic materials. This model took the binary phase diagrams of the ceramic materials into consideration and could analyze the phase change phenomena and flow motion in the melting pool. Xiao and Zhang [16] developed an even more comprehensive physical model in which a specific algorithm was developed to track the shrinkage in the powder bed. Recently, Luo et al. [21] built a three-dimensional transient finite element model to analyze the temperature and stress fields during the SLM of SnTe using ANSYS. Their model considered the latent heats associated with the melting and vaporization phenomena. However, their model did not incorporate the function of modeling the mass transfer process during the SLM simulation. Denlinger et al. [22,23] developed a three-dimensional finite element model to simulate the laser powder-bed fusion process. However, their approach couldn't model the fluid behavior which is critical to predict the impact of the process parameters on the fabricated material.

Magnesium silicide (Mg_2Si) is an inorganic compound having a face-centered cubic lattice structure. In its unit cell, it possesses the antifluorite structure with Si^{4-} ions occupying the corners and face-centered positions and Mg^{2+} ions occupying eight tetrahedral sites in the interior. The density of pure Mg_2Si is relatively low compared with other thermoelectric materials. Though the ZT value of Mg_2Si is slightly lower than Bi_2Te_3 , this material has many advantages over other materials because it is abundant, inexpensive, light-weighted, and nontoxic. A ZT value of ~ 1.4 was reported in Bi-doped Mg_2Si at 773 K with an average ZT of 0.9 between 400 and 773 K by Farahi et. [24], which was reasonably high for most thermoelectric applications. Furthermore, the mechanical properties of Mg_2Si are superior to those of PbTe for medium temperature application. Li et al. [25] demonstrated that thermoelectric and mechanical performance of Mg_2Si could be

significantly enhanced by nano-structuring via nonequilibrium syntheses, such as melt-spinning followed by spark plasma synthesis (SPS) or hot pressing. Zhang et al. [26] studied thermal spay of Mg₂Si and found that the points defects created by high quench rate helped to increase the ZT value. SLM based AM shared several merits with the thermal spray method, such as powder feeding, high quench rate, and high automation, but had important advantages over thermal spay by providing better process control for nanoparticle embedding, much higher mass density, milder fabrication conditions, less oxidation, and higher bonding strength. Zhang et al. [27] studied tthe effect of point defects and nanoparticles on thermal conductivity of Mg₂Si. Mg₂Si has been also used in the creation of metal matrix composites (MMC). Emamy et al. [28] et al. studied the properties of hot-extruded Al matrix composites (AMCs) containing different amounts of Mg₂Si, and found that the formation of separated dot-like Mg₂Si particles in hot extruded specimens eliminated the path for crack propagation and improved the ductility of the AMCs. Qin et al. [29] and Li at al. [30] investigated the growth manner of Mg₂Si particles in Mg₂Si/Al composite. They found that the final morphology of Mg₂Si crystal was affected by its intrinsic crystal structure and growth conditions. This phenomenon should be carefully considered during SLM fabrication.

In this paper, a 3D model based on the conservation law was developed to simulate the SLM manufacturing of Mg2Si powders embedded with nano-particles. This physical model, incorporating the ability to analyze the fluid flow driven by buoyancy force and surface tension, can be utilized to study the impact of the process parameters on the melting pool size, nanoparticle aggregation, and temperature profile in the powder bed. The governing equations – including the continuity, momentum, energy, and nanoparticle transport equations - were discretized using the finite volume method (FVM) and then solved in a pressure-based manner. The total variation diminishing (TVD) discretization scheme was used for all the governing equations to achieve second-order accuracy and unconditional stability. The alternating direction implicit (ADI) method and block correction method (BCM) was integrated with the SIMPLER algorithm to accelerate the convergence. The shrinkage phenomenon during the SLM fabrication was tracked using an adaptive grid method.

2. The physical model

2.1. The computational domain

The SLM process for thermoelectric powder fabrication modeled is shown in Fig. 2(a). SLM is a non-equilibrium manufacturing method, which can produce tremendous grain boundaries and defects within the sintered material. As shown in Fig. 2(b), a Gaussian laser beam moved over the powder bed with a velocity of U_b . The powders absorbed a partition of the laser energy and formed a liquid pool in which the unmelted nanoparticles could aggregate. The melting pool cooled down and solidified into a densified part after the laser beam moved away. As shown in Fig. 2(b), four distinct regions were identified in the powder bed: an un-sintered region, a sintered region, a mushy region, and a fluid region with dispersed nanoparticles. This system can be described by the conservation equations governing the transport of mass, momentum, energy, and nanoparticles. The computational domain had a size of 3.6 mm \times 1.2 mm \times 1.2 mm, which was much larger than the melting pool. The temperatures on the boundaries far away from the melting pool were assumed constant. Half of the powder bed was modeled to save half of the computational resource.

2.2. Governing equations

A single-phase model was adapted from the models illustrated in reference Voller et al. [20] with some modifications made to fit the current problem domain. Moreover, similar to the method used by Xiao and Zhang [16], the convective terms in the governing equations were

Fig. 2. (a) SLM manufacturing of multi-component thermoelectric powders with nanoparticles embedded. (b) Four distinct regions in the powder bed.

modified to fit the moving coordinates. The following assumptions were made to simplify the problem.

- a. The powder bed was assumed to be uniform in density. During the melting process, the gas in the porous structure was squeezed out gradually by the pressure introduced by the liquid. Finally, in the liquid region and the sintered region, the gas was completely ejected.
- b. The Boussinesq approximation was employed to calculate the buoyancy force caused by the density change.
- c. The powders have constant thermophysical properties, including the thermal conductivity, specific heat, viscosity, and diffusion coefficient. However, those values do not stay the same after the phase change.
- d. The shrinkage only influences the z-direction. Its impact on the x and y-directions was neglected.
- e. The simulations were only carried out for the first trail of SLM fabrication. However, not much effort is required to adapt the code to simulate the SLM process for multi-trail or other cases.

Considering an infinitesimally small fluid element fixed in space, we accounted the energy and mass flows through each face and built the continuity, momentum, energy, and nanoparticle equations based on the conservation law. The thermal properties were updated according to the phase and material compositions computed from the last iteration. The scanning speed of the laser beam remained constant (u_b) . The governing equations were accommodated to a single-phase model for all the regions of the computational domain in a moving coordinate system as follows.

The continuity equation:

$$\frac{\partial \rho}{\partial t} + \frac{\partial (\rho(u - u_b))}{\partial x} + \frac{\partial (\rho v)}{\partial y} + \frac{\partial (\rho w)}{\partial z} = 0$$
 (1)

The momentum equations in \boldsymbol{x} , \boldsymbol{y} , and \boldsymbol{z} directions:

$$\frac{\partial(\rho u)}{\partial t} + \frac{\partial[\rho u(u - u_b)]}{\partial x} + \frac{\partial(\rho uv)}{\partial y} + \frac{\partial(\rho uw)}{\partial z}
= -\frac{\partial p}{\partial x} + \frac{\partial}{\partial x} \left(\mu^{+} \frac{\partial u}{\partial x}\right) + \frac{\partial}{\partial y} \left(\mu^{+} \frac{\partial u}{\partial y}\right) + \frac{\partial}{\partial z} \left(\mu^{+} \frac{\partial u}{\partial z}\right)$$
(2)

$$\frac{\partial(\rho v)}{\partial t} + \frac{\partial[\rho v(u - u_b)]}{\partial x} + \frac{\partial(\rho vv)}{\partial y} + \frac{\partial(\rho vw)}{\partial z} \\
= -\frac{\partial p}{\partial y} + \frac{\partial}{\partial x} \left(\mu^+ \frac{\partial v}{\partial x}\right) + \frac{\partial}{\partial y} \left(\mu^+ \frac{\partial v}{\partial y}\right) + \frac{\partial}{\partial z} \left(\mu^+ \frac{\partial v}{\partial z}\right)$$
(3)

$$\begin{split} \frac{\partial(\rho w)}{\partial t} + \frac{\partial[\rho w(u - u_b)]}{\partial x} + \frac{\partial(\rho wv)}{\partial y} + \frac{\partial(\rho ww)}{\partial z} \\ &= -\frac{\partial p}{\partial z} \\ &+ \frac{\partial}{\partial x} \left(\mu^+ \frac{\partial w}{\partial x}\right) + \frac{\partial}{\partial y} \left(\mu^+ \frac{\partial w}{\partial y}\right) + \frac{\partial}{\partial z} \left(\mu^+ \frac{\partial w}{\partial z}\right) + \rho_{ref} g_r (T - T_e) (\beta_T + \beta_s C_s) \end{split}$$

The energy equation:

$$\frac{\partial(\rho h)}{\partial t} + \frac{\partial(\rho h(u - u_b))}{\partial x} + \frac{\partial(\rho h v)}{\partial y} + \frac{\partial(\rho h w)}{\partial z}
= \frac{\partial}{\partial x} \left(k^+ \frac{\partial T}{\partial x} \right) + \frac{\partial}{\partial y} \left(k^+ \frac{\partial T}{\partial y} \right) + \frac{\partial}{\partial z} \left(k^+ \frac{\partial T}{\partial z} \right) + S_h$$
(5)

The nanoparticle transport equation:

$$\frac{\partial(\rho C^{+})}{\partial t} + \frac{\partial(\rho C^{+}(u - u_{b}))}{\partial x} + \frac{\partial(\rho C^{+}v)}{\partial y} + \frac{\partial(\rho C^{+}w)}{\partial z}
= \frac{\partial}{\partial x} \left(D^{+} \frac{\partial C^{+}}{\partial x} \right) + \frac{\partial}{\partial y} \left(D^{+} \frac{\partial C^{+}}{\partial y} \right) + \frac{\partial}{\partial z} \left(D^{+} \frac{\partial C^{+}}{\partial z} \right) + S_{C}$$
(6)

where u, v, and w are the velocities in x, y, and z directions respectively, ρ is the density, p is the pressure, T is the temperature, h is the enthalpy, k^+ represents the effective thermal conductivity, μ^+ represents the effective viscosity, C^+ represents the nanoparticle concentration, D^+ represents the effective diffusion coefficient, S_C and S_h are the source terms for the energy and nanoparticle transport equations, respectively, β_T and β_s are the liquid and solid thermal expansion coefficients, respectively, and C_s is the solid mass concentration. Eqs. (1)–(6) should be solved together, as all the parameters were strongly coupled. The fluid field in the melting pool were driven by the buoyance force and surface tension. The buoyance force was a volume effect, which was modeled by the last source term of Eq. (4). The surface tension was a boundary effect. The enthalpy or temperature change during the phase transition was described by the last source terms of Eq. (5). The nanoparticle concentration variation caused by the phase transition was given by the last source terms of Eq. (6). The details of each equation were explained as follows.

Since the Si nanoparticles had a relatively small thermal expansion coefficient and mass concentrations, they had a relatively small influence over buoyancy force. Therefore, in Eq. (4), its effect over solid expansion was neglected. Similar to the treatment in reference [16], the relative velocity (w_s) to the coordinate introduced by shrinkage could be calculated by:

$$w_{s} = \begin{cases} 0, & z \ge s \\ \varepsilon \left(\frac{\partial s}{\partial t} - u_{b} \frac{\partial s}{\partial x} \right), & z < s \end{cases}$$
 (7)

The powders started to melt at $T_M - \Delta T$, and melted completely at a temperature of T_M . Also, it was assumed that the mass fraction of the liquid increased with the temperature in this temperature window.

$$f_{l} = \left\{ \begin{array}{ll} 1, & T \geq T_{M} \\ \frac{T_{M} - T}{\Delta T}, & T_{M} - \Delta T < T < T_{M} \\ 0, & T \leq T_{M} - \Delta T \end{array} \right\}$$
(8)

The physical properties of the partially melted powders in the mushy region were simplified as the summation of the properties of the powders and liquid weighted by the corresponding mass fractions. Based on this assumption, the effective viscosity and the effective thermal conductivity were calculated by Eqs. (9) and (10) as follows.

$$\mu^+ = \mu f_s + \mu f_l \tag{9}$$

$$k^+ = f_s k_s + f_l k_l \tag{10}$$

The powders used in the process were not completely pure. Doping materials and nanoparticles were added in the powders to enhance the ZT value. Similar to the treatment above, the thermal conductivity of the mixture (k_p) could be estimated as the summation of the thermal conductivity (k_{pi}) of the different powder components weighted by their corresponding mass fractions (g_{pi}) .

$$k_p = \sum_{i=1}^n g_{pi} k_{pi} \tag{11}$$

An empirical equation built by Hadley [31] and further outlined by Xiao and Zhang [16] was utilized to estimate the effective thermal conductivity of the porous powder bed. The equation can be used to calculate the effective thermal conductivity of a porous material whose solid fraction has a much higher thermal conductivity than its gas fraction with reasonable accuracy.

$$\frac{k_{eff}}{k_g} = (1 - \alpha_0) \frac{\varepsilon f_0 + (k_p/k_g)(1 - \varepsilon f_0)}{1 - \varepsilon (1 - f_0) + \varepsilon (k_p/k_g)(1 - f_0)} + \alpha_0 \frac{2(k_p/k_g)^2 (1 - \varepsilon) + (1 + 2\varepsilon)(k_p/k_g)}{(2 + \varepsilon)(k_p/k_g) + 1 - \varepsilon}$$
(12)

where

$$f_0 = 0.8 + 0.1\varepsilon,\tag{13}$$

$$\log \alpha_0 = \begin{cases} -4.898\varepsilon & 0 \le \varepsilon \le 0.0827\\ -0.405 - 3.154(\varepsilon - 0.0827) & 0.0827 \le \varepsilon \le 0.298\\ -1.084 - 6.778(\varepsilon - 0.298) & 0.298 \le \varepsilon \le 0.580 \end{cases}$$
 (14)

The nanoparticle concentration in the original powders was C_s . The nanoparticle concentration in the solid and the liquid were related through $C_s = \varphi C_l$. The effective nanoparticle diffusive coefficient of the powder was estimated by

$$D^+ = f_s D_s + f_l D_l / \varphi \tag{15}$$

The thermal capacity of the powders was temperature-dependent. The integration of thermal capacity gave the enthalpy of the powders.

$$h = \int_0^T c_{ps} dT \tag{16}$$

The enthalpy changes during the phase transition consisted of two parts: the thermal capacity change and the latent heat.

$$\delta H = \left[\int_0^T (c_{pl} - c_{ps}) dT + L \right] f_l \tag{17}$$

It was assumed that the thermal capacity of the sintered material did not change during the SLM fabrication, thus the Eq. (17) was simplified as

$$\delta H = \begin{cases} 0, & T < T_M - \Delta T \\ Lf_l, & T_M - \Delta T < T < T_M \\ L, & T > T_M - \Delta T \end{cases}$$
 (18)

The melting temperature of the Mg_2Si is 1375 K, and the melting temperature of Si is 1687 K. The Si nanoparticle had a much higher melting temperature than the Mg_2Si matrix. In this model, the Si nanoparticles were assumed maintaining solid during the SLM fabrication. The enthalpy of the powder bed would not be affected by the nanoparticle concentration because Si nanoparticles didn't experience phase transition. However, the temperature field of the melting pool was still changed by the nanoparticles, as the nanoparticle concentration

distribution in the pool was not uniform. The expression of the source term for the energy equation was given by Eq. (19). The first term of the Eq. (19) was the transient term. And the other terms were caused by the energy convection associated with the mass transport in the melting pool.

$$S_{h} = \frac{-\partial}{\partial t}(\rho \delta H) - \frac{\partial}{\partial x}(\rho(u - u_{b})\delta H) - \frac{\partial}{\partial y}(\rho v \delta H) - \frac{\partial}{\partial z}(\rho w \delta H)$$
(19)

The expression of the source term for the nanoparticle transport equation is given by Eq. (20). The first term on the right hand of Eq. (20) is the transient term caused by the melting and re-solidification of the powders. The other terms were introduced to account for the mass convection.

$$S_{C} = \frac{-\partial}{\partial t} \left[\left(\frac{1}{k} - 1 \right) \rho f_{1} C_{s} \right] - \frac{\partial}{\partial x} \left[\left(\frac{1}{k} - 1 \right) \rho f_{1} C_{s} (u - u_{b}) \right] - \frac{\partial}{\partial y} \left[\left(\frac{1}{k} - 1 \right) \rho f_{1} C_{s} w \right]$$

$$- 1 \right) \rho f_{1} C_{s} v \right] - \frac{\partial}{\partial z} \left[\left(\frac{1}{k} - 1 \right) \rho f_{1} C_{s} w \right]$$

$$(20)$$

2.3. Shrinkage on the powder bed

After the powders were melted, the capillary effect and gravity force would drive the liquid to take the gap place between the powders. Therefore, a shrinkage would happen because of the density difference between the powders and the liquid. In this paper, four sub-stages were set to represent the different status of the materials in the heating process (Fig. 3).

Stage One: pre-heating $(T < T_M - \Delta T)$.

In this stage, the melting point was not reached. No melting happened until the next stage in the fabrication process.

Stage Two: Preliminary melted
$$(T_M - \Delta T \le T \le T_M - \Delta T \frac{\varepsilon}{1-\varepsilon})$$
.

In this stage, only a small partition of the powders was melted. The liquid took up a partition of the gap which used to be filled by gas. The volume of the powders melted in a local grid was given by $f_l(1-\varepsilon)dxdydz$. As the gas was not completely driven out in the powder bed, all the powders melted would be used to fill the powder gap, which was given by

$$\Delta S_2 = f_l(1 - \varepsilon) dx dy dz \tag{21}$$

Stage Three: Partially melted $(T_M - \Delta T \frac{\varepsilon}{1-\varepsilon} < T < T_M)$.

In this stage, the gap in the powders was filled by the liquid. Thus, the melting would not cause further shrinkage. The shrinkage volume was equal to the powder porosity ε .

$$\Delta S_3 = \varepsilon dx dy dz \tag{22}$$

Stage Four: Fully melted $(T \ge T_M)$.

In this stage, all the powders were melted. The density variation during the phase change was neglected. No further shrinkage would happen in this stage.

$$\Delta S_4 = \varepsilon dx dy dz \tag{23}$$

2.3.1. Accumulated shrinkage

The accumulated shrinkage in the powder bed was calculated by integrating the shrinkage of each cell along the z-direction.

$$s = \left(\sum_{T_M - \Delta T}^{T_M - \Delta T + \frac{1 - \epsilon}{\epsilon}} \Delta S_2 + \sum_{T_f}^{T_M} \Delta S_3 + \sum_{T_M}^{T_{MAX}} \Delta S_4 \right) / (dxdy)$$
 (24)

2.4. The boundary conditions

Boundary A (top surface in Fig. 4): The laser power was absorbed by the powders. A part of the absorbed energy was lost to the ambient through convection and radiation. The heat convection coefficient and

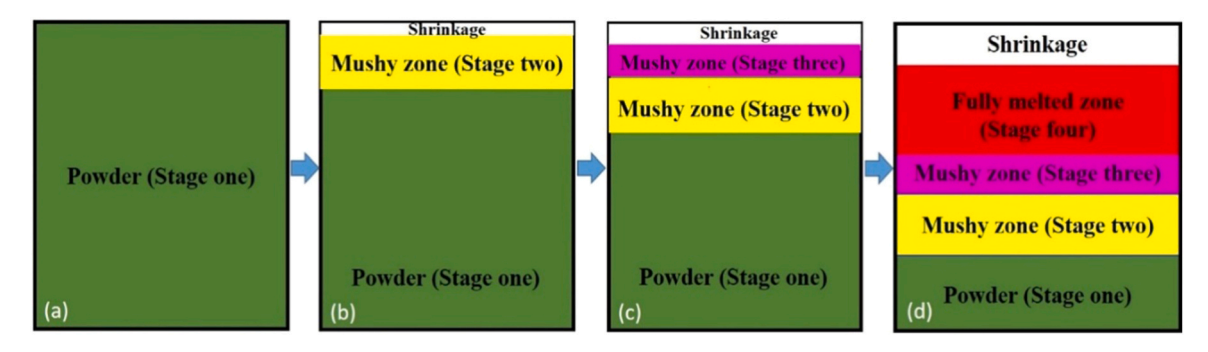


Fig. 3. The shrinkage phenomenon in the powder bed during the SLM process: (a) Stage One, (b) Stage Two, (c) Stage Three, and (d) Stage Four.

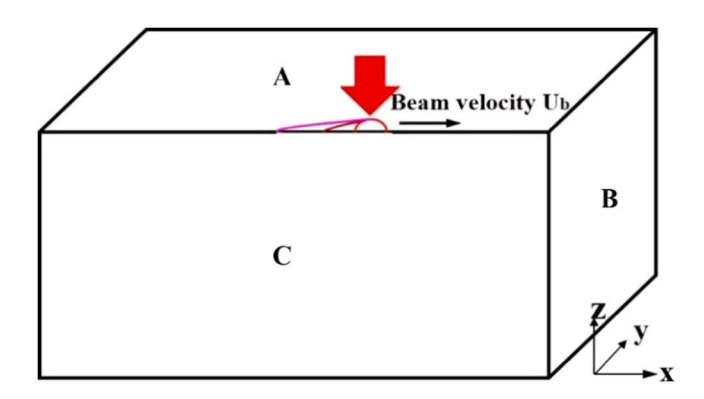


Fig. 4. The boundaries of the computation domain.

radiation emissivity can be affected by many factors. The values of heat convection coefficient and radiation emissivity were adopted from some recent literature [11,32] for simplicity.

$$-k_{eff}\partial T/\partial z|_{z=s} = \theta q_{laser} + h_c(T - T_a) + \varepsilon_b \sigma_b \left(T^4 - T_a^4\right)$$
 (25)

$$\theta = \begin{cases} 0, & Laserheatingspot \\ 1, & Topsurface except for laserheating spot \end{cases}$$
 (26)

The heat flux of the laser was assumed to be Gaussian.

$$q_{laser} = -\frac{q_0}{\pi R^2} exp\left(-\frac{r^2}{R^2}\right) \tag{27}$$

It was assumed that the shear force and surface tension at the free surface reached a balance.

$$\mu^{+}(\partial v_{s_1}/\partial n_1 + \partial v_{n_1}/\partial s_1) = \sigma_{s_1} \frac{\partial T}{\partial s_1} \quad (zzplane)$$
 (28)

$$\mu^{+}(\partial v_{s_2}/\partial n_2 + \partial v_{n2}/\partial s_2) = \sigma_{s_2} \frac{\partial T}{\partial s_2} \quad (yzplane)$$
 (29)

The nanoparticle concentration gradient was zero at this boundary.

$$\partial C^+/\partial z|_{z=s}=0 \tag{30}$$

Boundary B (the right, left, and bottom surfaces in Fig. 4):

The side and bottom surfaces were set far away enough from the laser heating point. Moreover, the thermal conductivity of the powder bed was small for the thermoelectric materials. The temperature fluctuations on these boundaries were negligible. The constant temperatures were assumed on these surfaces.

$$T = T_a \tag{31}$$

No particle motion was assumed on the boundary. The nanoparticle concentration gradient was zero.

$$u = v = w = 0 \tag{32}$$

$$\left. \frac{\partial C^+}{\partial x} \right|_{z=0,L} = 0 \tag{33}$$

Boundary C (the upfront surface in Fig. 4): It is a symmetrical surface.

$$\partial T/\partial y|_{y=0} = 0 \tag{34}$$

$$v = 0, \quad \frac{\partial u}{\partial y} = \frac{\partial w}{\partial y} = 0 \tag{35}$$

$$\partial C^+/\partial y|_{y=0} = 0 \tag{36}$$

2.5. Numerical algorithm

The SLM process was a three-dimensional quasi-steady state heat and mass transfer problem in a moving coordinate system. The SIMPLER algorithm developed by Patankar [33] was used to solve the governing equations presented in Section 2.2 numerically. The material properties were updated according to the temperature profile updated from the last iteration. Since the shrinkage of the powder bed was unknown beforehand, the shrinkage profile was updated each time step by a false transient method. The solution was assumed to converge when the velocity and temperature distributions did not change with time. A TVD scheme proposed by Van Leer [34] was utilized to discretize the convection and diffusion terms. The TVD scheme was of second-order accuracy and unconditionally stable without overshoot. The limiter function for this TVD scheme was given by Eq. (37).

$$\psi(r) = \frac{r + |r|}{1 + r} \tag{37}$$

The discretization scheme documented in Versteeg and Malalasekera's book [35] for the two-dimensional system was extended to the three-dimensional Cartesian grid system.

$$a_{P}\phi_{P} = a_{W}\phi_{W} + a_{E}\phi_{F} + a_{S}\phi_{S} + a_{N}\phi_{N} + a_{F}\phi_{F} + a_{B}\phi_{R} + S_{u}^{DC} + S_{\phi}$$
(38)

where the central coefficient was $a_P = a_W + a_E + a_S + a_N + a_F + a_B + (F_e - F_w) + (F_n - F_s) + (F_b - F_f)$ and a_W , a_E , a_S , a_N , a_F and a_B were the TVD neighbor coefficients.

The deferred correction source term was given by

$$S_{u}^{DC} = \frac{1}{2} F_{e} \left[(1 - \alpha_{e}) \psi(r_{e}^{-}) - \alpha_{e} \psi(r_{e}^{+}) \right] (\phi_{E} - \phi_{P}) + \frac{1}{2} F_{w} \left[- (1 - \alpha_{w}) \psi(r_{w}^{-}) + \alpha_{w} \psi(r_{w}^{+}) \right] (\phi_{P} - \phi_{W}) + \frac{1}{2} F_{n} \left[(1 - \alpha_{n}) \psi(r_{n}^{-}) - \alpha_{n} \psi(r_{n}^{+}) \right] (\phi_{N} - \phi_{P}) + \frac{1}{2} F_{s} \left[- (1 - \alpha_{s}) \psi(r_{s}^{-}) + \alpha_{s} \psi(r_{s}^{+}) \right] (\phi_{P} - \phi_{S}) + \frac{1}{2} F_{b} \left[(1 - \alpha_{b}) \psi(r_{b}^{-}) - \alpha_{b} \psi(r_{b}^{+}) \right] (\phi_{B} - \phi_{P}) + \frac{1}{2} F_{f} \left[- (1 - \alpha_{f}) \psi(r_{f}^{-}) + \alpha_{b} \psi(r_{f}^{+}) \right] (\phi_{P} - \phi_{B})$$
(39)

where $r_e^+, r_e^-, r_w^+, r_w^-, r_n^+, r_n^-, r_s^+, r_s^-, r_b^+, r_b^-, r_f^+$, and r_f^- were defined as the local ratios of the upstream gradient to the downstream gradient, and

the superscripts ('+' and'-') represented the flow directions.

The thermal boundaries were treated using the additional source term method. A grid system with uniformly structured hexahedron grids, $200 \times 90 \times 90$ in the x,y, and z directions, were adopted for the modeling. The false time step was set as 0.0001 s to make sure CFL < 1.0 for all the grids. The iterative procedure continued until the residuals of all the governing equations were less than 10^{-5} . The solution was assumed to be converged when $\left|\frac{\phi_N-\phi_{N-1}}{\phi_N}\right| < 10^{-3}$. The BCM described in Tao's book [36] and the ADI method were employed to accelerate the convergence. (Fig. 5).

2.6. Material physical properties and input parameters

In this SLM simulation, the Mg₂Si powders were chosen to be the working powders. A small proportion of the silicon nanoparticles were added into the powder to enhance both the thermoelectric performance and the mechanical properties of the final product [27]. Akasaka et al. [37] measured the thermal conductivity of the Mg₂Si bulk material in a wide temperature range. The effective thermal conductivity of the Mg₂Si powders was calculated based on the Mg₂Si bulk material using Eq. (12). As for other physical properties, including the thermal capacity and the thermal expansion coefficient, data from Yu's paper [38] was used. The doping ratio of silicon particles was set at 10%. Glassbrenner and Slack [39] gave the detailed physical properties of silicon bulk material, which were adopted for the simulation in this paper. The material properties of the nanoparticles were different from the bulk materials. The difference can be significant when the sizes of the particles approach to tens of nanometers [40]. The size effect on the material properties was not considered in this model. A more comprehensive model should take quantum effect into consideration. The material properties and the process parameters used in this paper were listed in Table 1.

3. Results and discussion

3.1. Code validation

Before modeling the SLM fabrication of the thermoelectric materials, the in-house code was first employed to simulate the SLM fabrication of

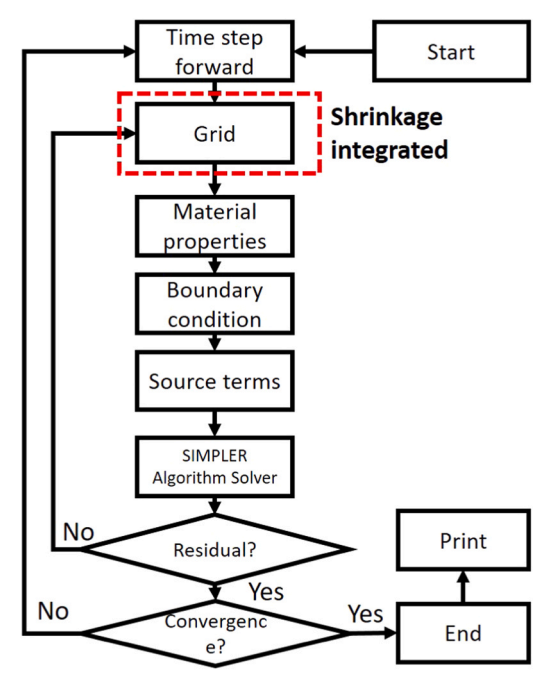


Fig. 5. The numerical scheme for SLM simulation.

Table 1 The material properties of the Mg_2Si powders and SLM operation conditions.

Scanning speed	$u_b = 0.01 - 0.2 \cdot ms^{-1}$
Specific heat	$c_p = 67.87 J \cdot kg^{-1} K^{-1} [38,39]$
Solid thermal conductivity	$k_p = 7.0 \ W \cdot m^{-1} \cdot K^{-1} [37,39]$
Liquid thermal conductivity	$k_l = 5.0 \ W \cdot m^{-1} \cdot K^{-1} [37,39]$
Gas thermal conductivity	$k_{\rm g} = 0.024 \ W \cdot m^{-1} \cdot K^{-1} [31]$
Porosity	$\varepsilon=0.2$ (variable)
Density	$ ho = 1990 kg \cdot m^{-3} [38]$
Liquid viscosity	$\mu_l = 5.0 \times 10^{-3} \ kg\cdot m^{-1} \cdot s^{-1} [38]$
Solid viscosity	$\mu_s = 1.0 \times 10^4 kg \cdot m^{-1} \cdot s^{-1} [16]$
Specific diffusion coefficient	$D = 4.8 \times 10^{-9} m^2 \cdot s^{-1} [16]$
Latent heat	$L = 4.5 \times 10^5 J \cdot kg^{-1} [38]$
Permeability coefficient	$K_0 = 2.0 \times 10^6 kg \cdot m^{-3} \cdot s^{-1} [16]$
Thermal expansion coefficient	$\beta_T = 1.1 \times 10^{-5} K^{-1} [38]$
Melting point of pure material	$T_M=1375K[38]$
Equilibrium partition ratio	k=0.8[16]
Ambient temperature	$T_a = 298.15K$
Convective heat transfer coefficient	$h_c = 10.0 \ W \cdot m^{-2} \cdot K^{-1} [11,16]$
Laser diameter	R = 0.3 mm (variable)
Laser power	Q=18.75-25~W
Boltzmann constant	$\sigma_b = 5.67 \times 10^{-8} \ W \cdot m^{-2} \cdot K^{-4}$
Change rate of surface tension	$\partial \sigma/\partial T = -10^{-5} kg \cdot s^{-2} \cdot K[16]$
Radiation emissivity	$\varepsilon_b = 0.86[32]$

a nonporous 6063 aluminum sheet. The dimension of the computational domain was 229 mm \times 152 mm \times 3.2 mm. Kou and Wang [41] conducted an experiment to process the nonporous aluminum sheet with a continuous-wave CO2 laser. The laser beam had a diameter of 0.6 mm, a power of 1.3 kW. For this specific case, it moved over the powder bed at a scanning speed of 4.23 mm/s. The energy profile of the laser beam was measured to be similar to Gaussian distribution. Kou and Wang [32] calorimetrically measured the power absorbed by the workpiece. The measurement found that about 86% of laser energy was lost to the environment through laser reflection, heat convection, and thermal radiation. In this simulation, the physical properties of the nonporous 6063 aluminum and the boundary conditions were set the same to the literature [41]. Before this code was used for modeling, a grid independence check was done to validate the code. As shown in Fig. 6, the simulated fusion boundaries for all the three grid systems matched each other very well. To further validate this code, the modeling results were compared with the simulation results [16] and experimental results [32] that documented in the open literature (Fig. 7). It showed that the

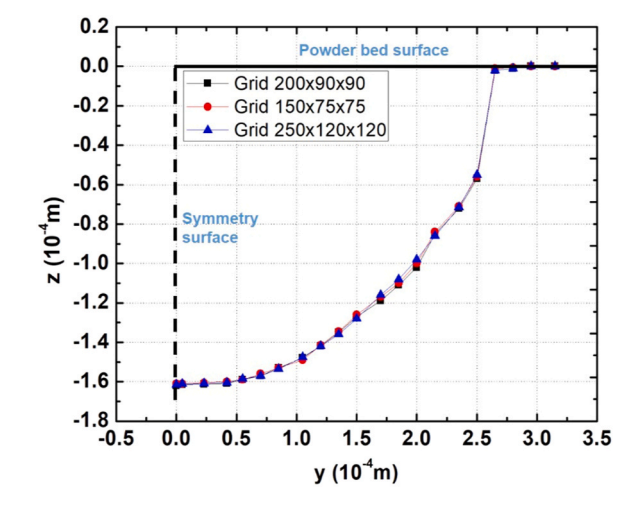


Fig. 6. The comparison of the simulated fusion boundaries with different grid systems.

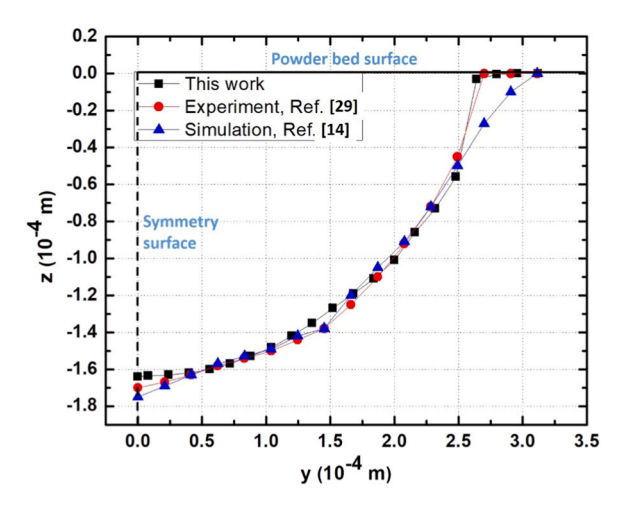


Fig. 7. The comparison of the simulated and measured fusion boundaries.

simulated and measured fusion boundaries were in good agreement with each other.

3.2. Shrinkage in the powder bed

After validation, the code was used to model the SLM fabrication of the thermoelectric material. Fig. 8 shows the shrinkage regions in the powder bed with different laser power inputs and scanning speeds. The energy input here was the energy absorbed by the powders. The maximum shrinkage depth was about 0.06 mm for an energy input of 18.75 W. With an increase in the input power, the shrinkage region became broader and deeper. The scanning speed also affected the shrinkage of the powder bed. The higher scanning speed yielded uniform temperature and thus led to more extensive and shallow shrinkage on the powder bed. Because of the shrinkage phenomenon, the surface roughness of the fabricated layer was difficult to control which would influence the electrical and thermal contact resistance between the fabricated layers. As a result, the ZT value of the sintered thermoelectric

material would be reduced. To reduce the shrinkage of the powder bed, the porosity of the powder bed should be as low as possible. Meanwhile, an appropriate laser power should be selected, since too small energy input could not melt the powder while too large energy input resulted in significant powder shrinkage, severe evaporation, and substantial deposited layer overlap. Finally, the scanning speed should be adjusted according to the laser energy input. For a high power laser, the scanning speed should be higher to alleviate the potential evaporation and oxidation caused by the high temperature. An appropriate laser power should be chosen based on the material properties, scanning speed, and laser diameter. It was possible to choose a set of parameters that enable part fabrication while avoiding evaporation. For example, in a recent literature, Mao et al. [13] conducted a series of experiments to identified the optimal processing window for Bi₂Te_{2.7}Se_{0.3}, another thermoelectric material. In their paper, it was found that the laser power and scanning speed were the two critical parameters that affected the surface morphologies of SLM-prepared layers. The laser power input and the scanning speed should be calibrated synchronously to fabricate Mg2Si material with optimal thermoelectric performance.

3.3. Temperature profile

Shown in Fig. 9 were the temperature profiles on the upper surface of the powder bed during the SLM process. A high-temperature spot was generated by the laser heating of the powder bed. As the laser beam moved from the left side to the right side, a high-temperature tail was left behind the laser. The high temperature happened near the center of the laser on the surface of the powder bed with a peak temperature ranging 1200–2500 K with laser power varying from 6.5 W to 25.0 W. The peak temperature created by the laser was much lower than the boiling temperature of Mg₂Si and Si, thus the evaporation effect could be neglected for these cases. With the laser input energy increasing, the high-temperature region expanded gradually. Since the peak temperature of the heating surface was significantly higher than the melting temperature, undesired evaporation and oxidation might happen during the SLM fabrication of thermoelectric materials. The laser power should be carefully selected to avoid severe evaporation and oxidation. The

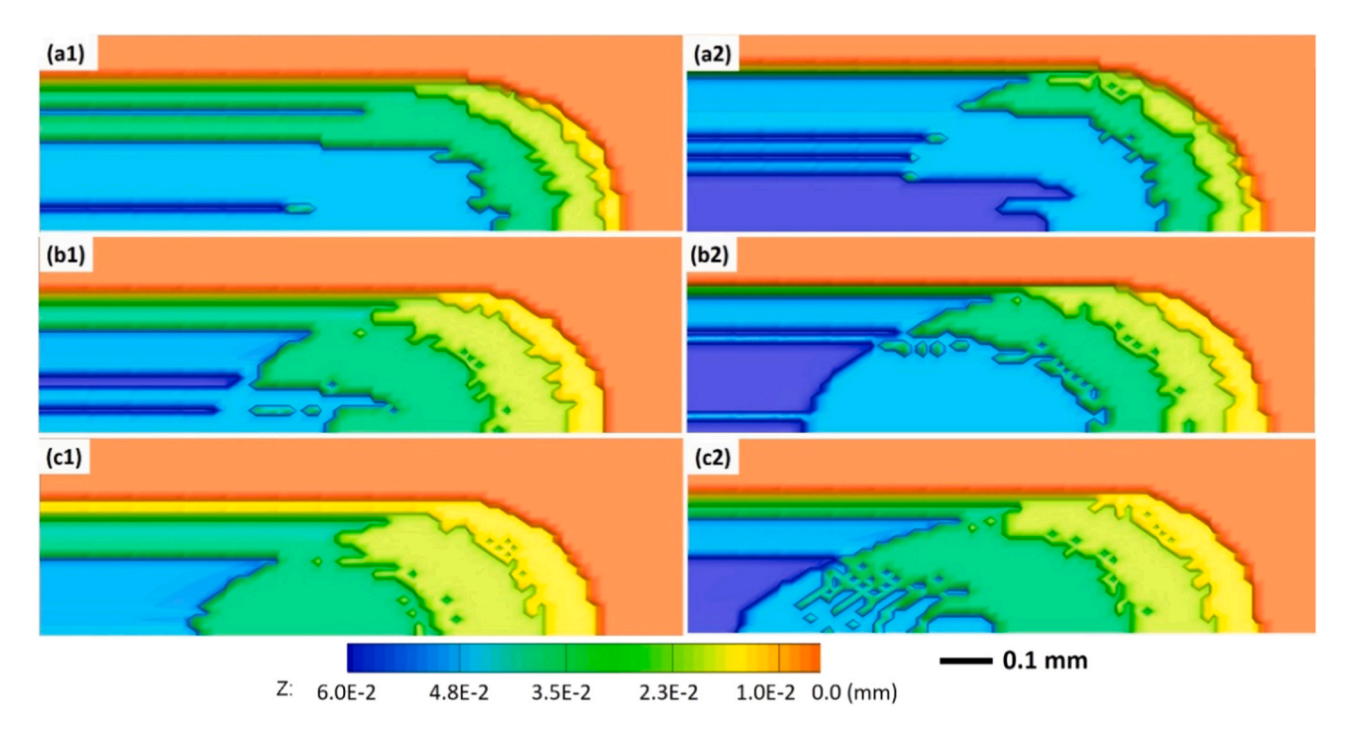


Fig. 8. The shrinkages of the powder bed. P = 18.75 W, R = 0.3 mm, (a1) V = 0.02 m/s; (b1) V = 0.04 m/s; (c1) V = 0.06 m/s. P = 25 W, R = 0.3 mm, (a2) V = 0.02 m/s; (b2) V = 0.04 m/s; (c2) V = 0.06 m/s.

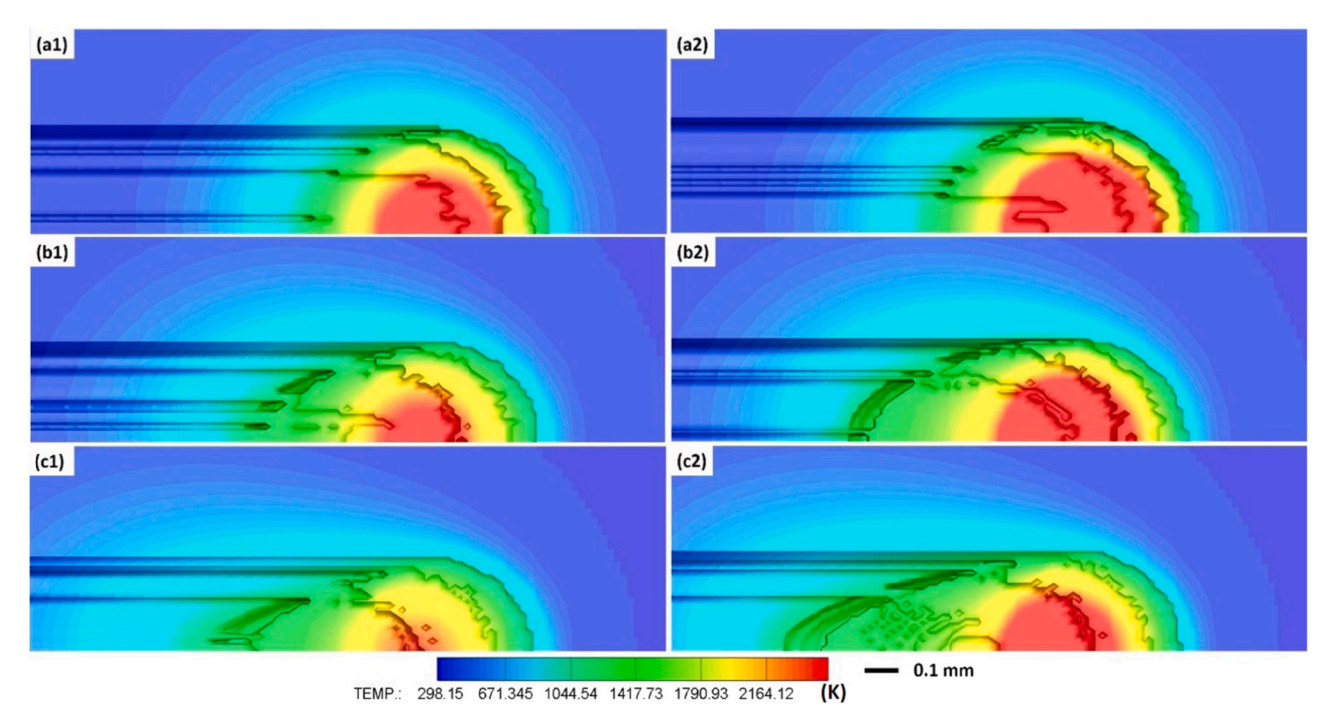


Fig. 9. The temperature profiles. P = 18.75 W, R = 0.3 mm, (a1) V = 0.02 m/s; (b1) V = 0.04 m/s; (c1) V = 0.06 m/s. P = 25 W, R = 0.3 mm, (a2) V = 0.02 m/s; (b2) V = 0.04 m/s; (c2) V = 0.06 m/s.

Table 2The average temperature of the heating spot for different processing conditions.

		Laser scanning speed				
		0.02 m/s	0.04 m/s	0.06 m/s	0.08m/s	0.1 m/s
	6.25 W	1175.2 K	1189.0 K	1129.7 K	1065.8 K	1005.4 K
Laser	12.5 W	1563.1 K	1482.4 K	1418.9 K	1345.3 K	1294.8 K
power	18.75 W	1893.2 K	1773.6 K	1706.2 K	1678.0 K	1622.3 K
	25.0 W	2075.6 K	1943.2 k	1881.3 K	1752.7 K	1701.6 K

		Laser scanning speed					
		0.02 m/s	0.04 m/s	0.06 m/s	0.08m/s	0.1 m/s	
	6.25 W	1175.2 K	1189.0 K	1129.7 K	1065.8 K	1005.4 K	
Laser	12.5 W	1563.1 K	1482.4 K	1418.9 K	1345.3 K	1294.8 K	
power	18.75 W	1893.2 K	1773.6 K	1706.2 K	1678.0 K	1622.3 K	
	25.0 W	2075.6 K	1943.2 k	1881.3 K	1752.7 K	1701.6 K	

laser scanning speed could be another factor that significantly affected the temperature distribution within the melting pool. The higher the scanning speed, the more extended high-temperature wake was observed. For the same laser energy input, the higher scanning speed resulted in a lower peak temperature. The average temperatures of the heating spot for different processing conditions were listed in Table 2. To melt the Mg₂Si powders selectively, the temperature of the heating spot should higher than the melting point of Mg₂Si (1375 K) and lower than the melting point of Si (1687 K). According to the modeling result, the temperature gradient at the center of the heating spot was in the order of 10^7 K/m and the temperature change rate could be as high as 6.0×10^5 K/s. The high stress caused by the high temperature gradient should be carefully monitored during the SLM fabrication. By calibrating the

scanning speed and the laser power, one could find the best processing parameters for Mg₂Si powder fabrication.

3.4. Melting pool size

The melting pool size played a vitally important role in SLM fabrication. The pool fluid dynamics in the melting pool could significantly affect the quality of the products. The size of the melting pool was directly correlated with the temperature profile. The melting pool sizes for cases with different energy inputs and scanning speeds are presented in Fig. 10. The red region is the liquid, the green region is the solid powders, and the blue region in between is the partially melted powders. It was observed that the higher energy input generated the larger the

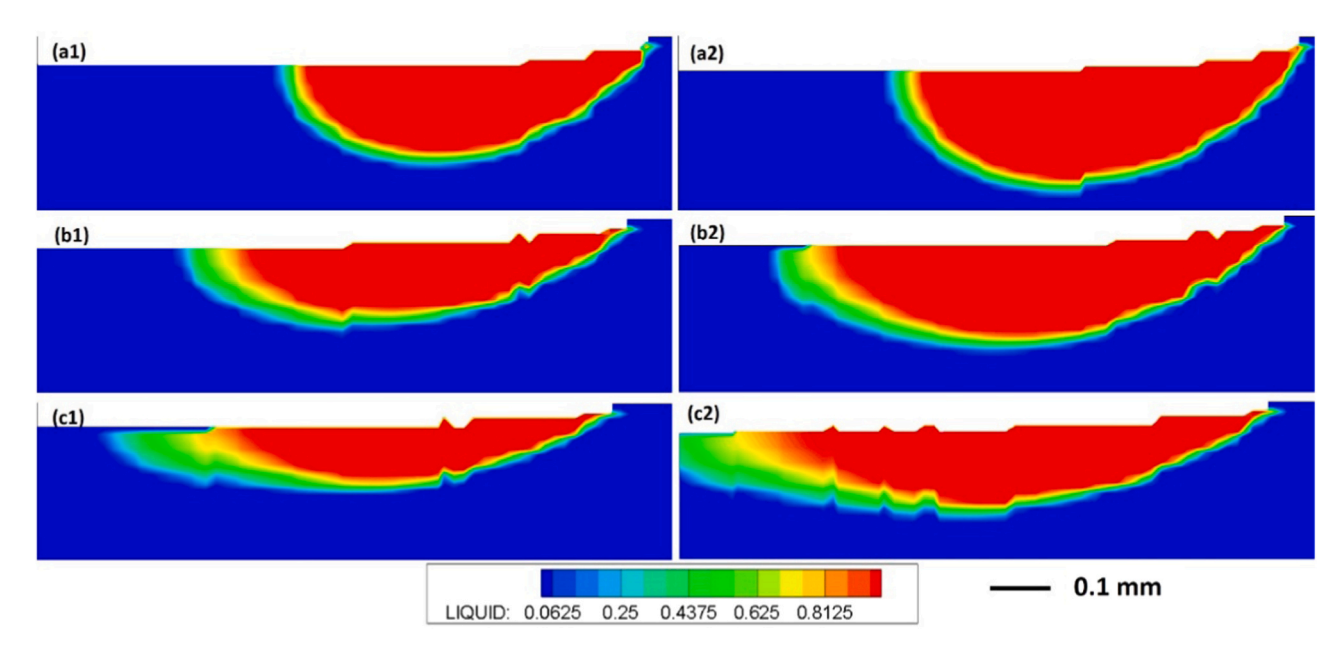


Fig. 10. The melting pool size. P = 18.75 W, R = 0.3 mm, (a1) V = 0.02 m/s; (b1) V = 0.04 m/s; (c1) V = 0.06 m/s. P = 25 W, R = 0.3 mm, (a2) V = 0.02 m/s; (b2) V = 0.04 m/s; (c2) V = 0.06 m/s.

melting pool. The shape of the melting pool changed accordingly with the scanning speed. The high scanning speed led to a narrow and long melting pool in the powder bed. The melting pool was not symmetrical on the front surface since the laser beam was moving from the left to the right. The asymmetry was more evident for the cases with the higher laser scanning speed. The melting pool size could significantly influence

the heat and mass transport in the pool. The buoyancy force and surface tension that drove the fluid motion in the melting pool primarily depended on the size of the melting pool. A large melting pool size should induce strong heat and mass convection which would accelerate the nanoparticle aggregation in the melting pool. Nanoparticles aggregation was undesired to achieve uniform physical properties and high

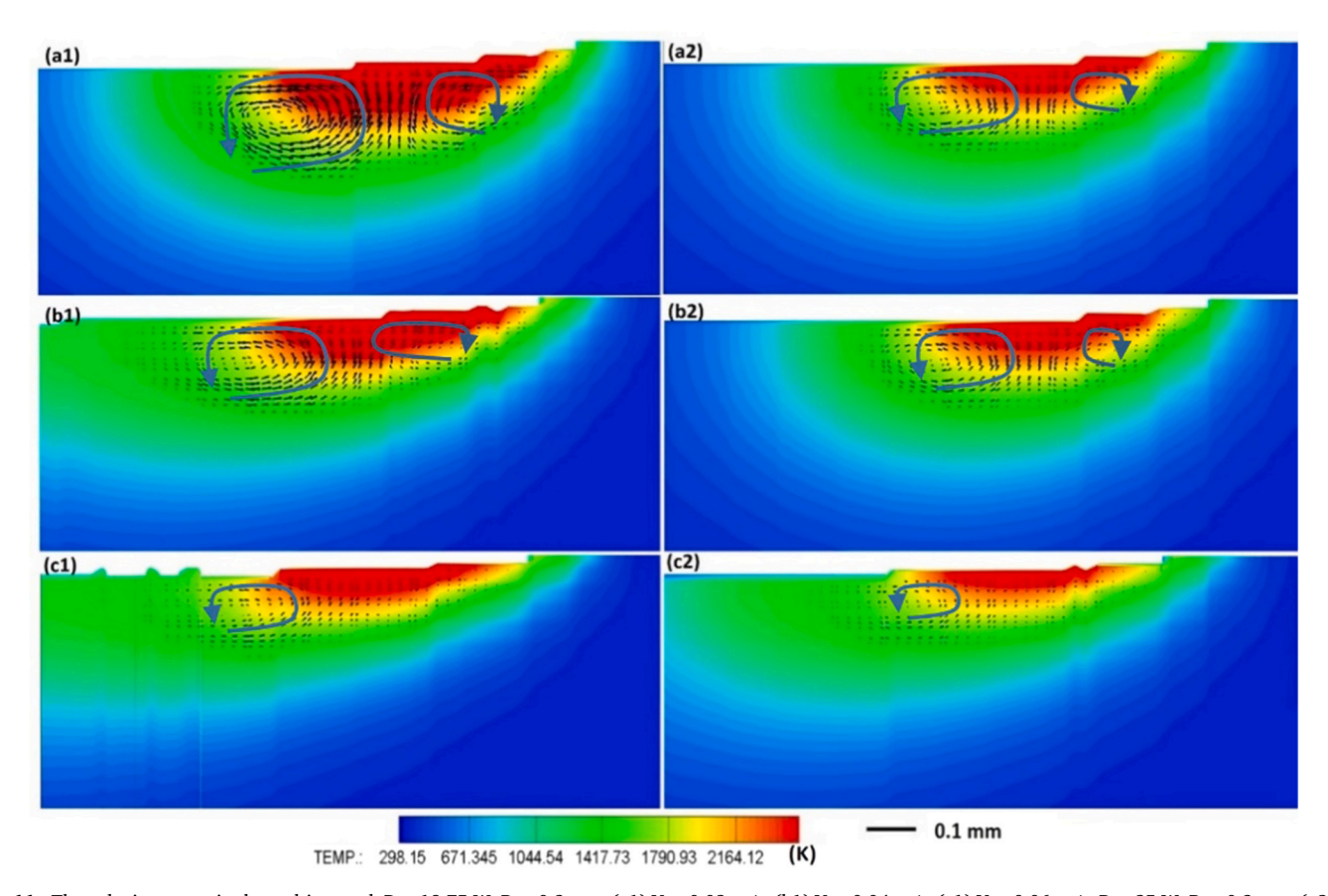


Fig. 11. The velocity vector in the melting pool. P = 18.75 W, R = 0.3 mm, (a1) V = 0.02 m/s; (b1) V = 0.04 m/s; (c1) V = 0.06 m/s. P = 25 W, P = 0.3 mm, (a2) V = 0.02 m/s; (b2) V = 0.04 m/s; (c2) V = 0.06 m/s.

thermoelectric performance in the final products. However, if the melting pool size was too small, the powders could not fully be melted, and the density of the final product would be too small to maintain good electrical conductivity, which is essential for good thermoelectric performance. The process parameters should be carefully selected to maintain an appropriate melting pool size.

3.5. Velocity profile

During the melting process, the temperature gradient on the free surface of the melting pool resulted in unbalanced surface tension along with the liquid-gas interface. Meanwhile, the density variation of the liquid generated a buoyancy force in the melting pool. The two forces drove the fluid to circulate in the melting pool. The peak velocity in the melting pool was on the order of 10^{-4} mm/s. Though the flow velocity was very small, it would accelerate nanoparticle aggregation in the sintered material which was undesired for thermoelectric material fabrication. Shown in Fig. 11 was the circulation pattern within the melting pool. It was observed that the surface tension force tended to pull the flow from the center to the edge of the melting pool, while the buoyancy force tended to drove the flow from the bottom to the top surface of the melting pool. The combined effect of these two forces created a flow circulation in the melting pool, where the flow ran up in the center and down on the edge of the melting pool. The circulation pattern at the front face was asymmetrical because the laser beam moved from right to the left over the powder bed. The high-temperature region on the left side of the laser beam was more extended and uniform because the heat flux absorbed by the powders diffused deeper to the powder bed. The asymmetrical temperature distribution led to an asymmetrical flow pattern in the melting pool. The left flow circulation was larger than the right half, and the difference became more significant for cases with higher scanning speed. The circulation pattern illustrated in Fig. 11 was consistent with the experimental [16,41] and simulation [16,41] results documented in the literature. It was also found that the circulation and convection within the melting pool became stronger with the higher power input. The convection process accelerated the mass transport processes during the fabrication. Its impact on the nanoparticle aggregation should be carefully monitored and controlled during the process.

3.6. Nano-particle concentration

Though the Si nanoparticles were uniformly mixed with the Mg₂Si powders, the nanoparticle distribution in the sintered material was no longer uniform anymore. As shown in Fig. 12, the nanoparticles aggregated on the boundary of the melting pool. The nanoparticle concentration near the melting pool was relatively small. This phenomenon happened because the solubility of the nanoparticles in the solid and liquid was different. The aggregation of the nanoparticles had a negative influence over the thermoelectric performance of the final products. The material composition ratio deviated from the optimum value. Even a small change in the composition ratio would significantly reduce the ZT value of the sintered thermoelectric material. During the SLM fabrication of the thermoelectric material, the process parameters should be carefully selected to suppress the aggregation of the nanoparticles. A potential way to combat this phenomenon is to shorten the residence time for material diffusion and convection by increasing the scanning speed. Other ways include reducing the input power to suppress the material diffusion and convection rates in the melting pool. However, increasing the scanning speed or reducing the input power could result in insufficient melting of the powders. There was an optimal processing parameter window for the SLM fabrication of Mg₂Si. According to the

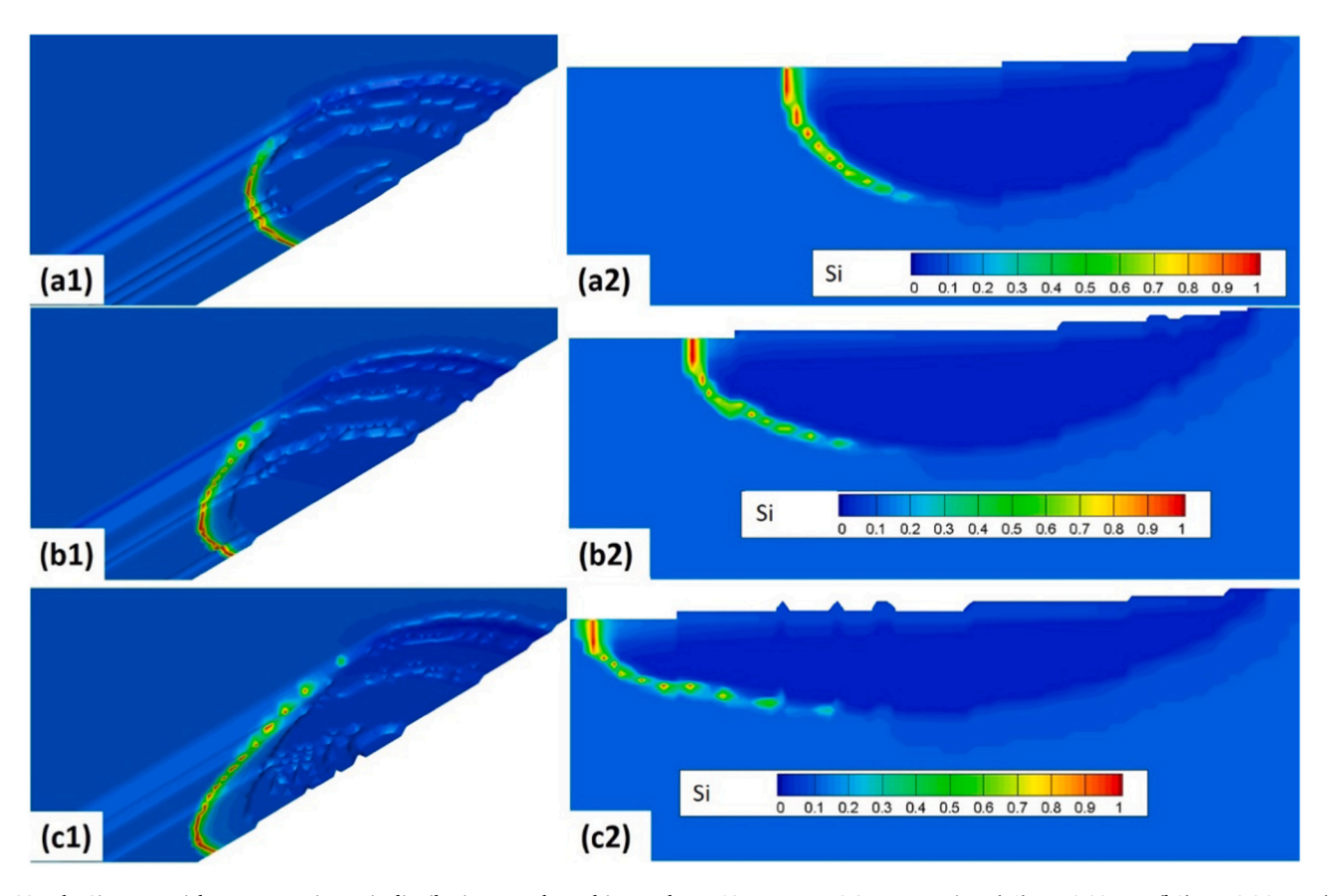


Fig. 12. The Si nanoparticles concentration ratio distribution near the melting pool. P=18.75~W, R=0.3~mm, top view: (a1) V=0.02~m/s; (b1) V=0.04~m/s; (c1) V=0.06~m/s; front view: (a2) V=0.02~m/s; (b2) V=0.04~m/s; (c2) V=0.06~m/s.

modeling result, with a laser diameter of $0.3 \, \text{mm}$, a laser power of $18.75 \, \text{W}$ and a scanning speed of $0.1 \, \text{m/s}$ were the best processing conditions for the SLM fabrication of Mg_2Si powders.

4. Conclusions

A comprehensive three-dimensional physical model was developed to simulate the SLM fabrication process of thermoelectric powders (Mg_2Si) embedded with nanoparticles (Si). This model was used to analyze the influence of the process parameters on sintered material. The shrinkage of the powder bed, the melting pool size and shape, the temperature and velocity profiles, and the nanoparticles concentration ratio in the powder bed during the SLM fabrication were compared for different laser power and scanning speed. The code was validated by checking the grid independence and examining a case reported in the literature before it was used for the thermoelectric material simulation.

- (1) Because of the porosity in the thermoelectric powder bed, a shrinkage region was observed during the SLM fabrication. The shrinkage depth and coverage area were larger for cases with larger power input. The scanning speed helped to make the temperature profiles uniform. The high scanning speed resulted in a long but shallow shrinkage region on the powder bed.
- (2) Both the energy input and the scanning speed had significant impacts on the melting pool. The energy input affected the size of the melting pool, while the scanning speed had more influence over the shape of the melting pool. By calibrating the scanning speed and the laser power, the suitable processing parameters for Mg2Si powder fabrication was identified.
- (3) The flow circulation in the melting pool was driven by the surface tension and the buoyancy force. Two opposite flow circulations were observed in the symmetric surface of the computational domain. The flow circulation pattern within the melting pool matched well with that reported in literature.
- (4) During the SLM fabrication, because of the difference in the solubility of Si nanoparticles in liquid and the Mg₂Si matrix, the Si nanoparticles tended to aggregate at the boundary of the melting pool. The doping level of the sintered material would deviate from the optimum value. The optimum processing conditions was suggested to solve this issue.

More experiments will be done in the future to calibrate this model.

Declaration of Competing Interest

The authors declare that they have no known competing financial interests or personal relationships that could have appeared to influence the work reported in this paper.

Acknowledgments

The authors gratefully acknowledge financial support from the US National Science Foundation via Grant #1915946 and the U.S. Department of Energy via Grant #16–10884.

References

- [1] D.M. Rowe. Thermoelectrics Handbook: Macro to Nano, CRC Press, 2005.
- [2] J.P. Kruth, P. Mercelis, J. Van Vaerenbergh, L. Froyen, M. Rombouts, Binding mechanisms in selective laser sintering and selective laser melting, Rapid Prototyp. J. 11 (1) (2005) 26–36.
- Y. Wu, J. Yang, S. Chen, L. Zuo, Thermo-element geometry optimization for high thermoelectric efficiency, Energy (2018).
 N. Mingo, D. Hauser, N.P. Kobayashi, M. Plissonnier, A. Shakouri, "Nanoparticle-
- [4] N. Mingo, D. Hauser, N.P. Kobayashi, M. Plissonnier, A. Shakouri, "Nanoparticle-in-Alloy" approach to efficient thermoelectrics: silicides in SiGe, Nano Lett. 9 (2) (2009) 711–715.
- [5] S.Y. Wang, J. Yang, T. Toll, J.H. Yang, W.Q. Zhang, X.F. Tang, Conductivitylimiting bipolar thermal conductivity in semiconductors, Sci. Rep. Uk 5 (2015).

- [6] B. Poudel, Q. Hao, Y. Ma, Y.C. Lan, A. Minnich, B. Yu, X.A. Yan, D.Z. Wang, A. Muto, D. Vashaee, X.Y. Chen, J.M. Liu, M.S. Dresselhaus, G. Chen, Z.F. Ren, High-thermoelectric performance of nanostructured bismuth antimony telluride bulk alloys, Science 320 (5876) (2008) 634–638.
- [7] A.J. Minnich, M.S. Dresselhaus, Z.F. Ren, G. Chen, Bulk nanostructured thermoelectric materials: current research and future prospects, Energy Environ. Sci. 2 (5) (2009) 466–479.
- [8] Y. Thimont, S. Leblanc, The impact of thermoelectric leg geometries on thermal resistance and power output, J. Appl. Phys. 126 (9) (2019), 095101.
- [9] A. Eldesouky, M.J. Carter, M.A. Andre, P.M. Bardet, S. Leblanc, Rapid processing and assembly of semiconductor thermoelectric materials for energy conversion devices, Mater. Lett. 185 (2016) 598–602.
- [10] A. El-Desouky, M. Carter, M. Mahmoudi, A. Elwany, S. LeBlanc, Influences of energy density on microstructure and consolidation of selective laser melted bismuth telluride thermoelectric powder, J. Manuf. Process 25 (2017) 411–417.
- [11] M.J. Carter, A. Eldesouky, M.A. Andre, P.M. Bardet, S. Leblanc, Pulsed laser melting of bismuth telluride thermoelectric materials, J. Manuf. Process 43 (2019) 35-46
- [12] N. Kang, P. Coddet, J. Wang, H. Yuan, Z.M. Ren, H.L. Liao, C. Coddet, A novel approach to in-situ produce functionally graded silicon matrix composite materials by selective laser melting, Compos. Struct. 172 (2017) 251–258.
- [13] Y. Mao, Y.G. Yan, K.P. Wu, H.Y. Xie, Z.K. Xiu, J.H. Yang, Q.J. Zhang, C. Uher, X. F. Tang, Non-equilibrium synthesis and characterization of n-type Bi2Te2.7Se0.3 thermoelectric material prepared by rapid laser melting and solidification, RSC Adv. 7 (35) (2017) 21439–21445.
- [14] Y. Yan, H. Ke, J. Yang, C. Uher, X. Tang, Fabrication and thermoelectric properties of n-Type CoSb2.85Te0.15 using selective laser melting, ACS Appl. Mater. Interfaces 10 (16) (2018) 13669–13674.
- [15] K. Wu, Y. Yan, J. Zhang, Y. Mao, H. Xie, J. Yang, Q. Zhang, C. Uher, X. Tang, Preparation of n-type Bi2Te3 thermoelectric materials by non-contact dispenser printing combined with selective laser melting, Phys. Status Solidi Rapid Res. Lett. 11 (6) (2017), 1700067.
- [16] B. Xiao, Y.W. Zhang, Marangoni and buoyancy effects on direct metal laser sintering with a moving laser beam, Numer. Heat Transf. A Appl. 51 (8) (2007) 715–733
- [17] J.P. Kruth, L. Froyen, J. Van Vaerenbergh, P. Mercelis, M. Rombouts, B. Lauwers, Selective laser melting of iron-based powder, J. Mater. Process Tech. 149 (1–3) (2004) 616–622.
- [18] C. Korner, E. Attar, P. Heinl, Mesoscopic simulation of selective beam melting processes. J. Mater. Process Tech. 211 (6) (2011) 978–987.
- [19] S.A. Khairallah, A. Anderson, Mesoscopic simulation model of selective laser melting of stainless steel powder, J. Mater. Process Tech. 214 (11) (2014) 2627–2636
- [20] V.R. Voller, A.D. Brent, C. Prakash, The modeling of heat, mass and solute transport in solidification systems, Int J. Heat. Mass Transf. 32 (9) (1989) 1719–1731.
- [21] C. Luo, J. Qiu, Y. Yan, J. Yang, C. Uher, X. Tang, Finite element analysis of temperature and stress fields during the selective laser melting process of thermoelectric SnTe, J. Mater. Process Tech. 261 (2018) 74–85.
- [22] E.R. Denlinger, M. Gouge, J. Irwin, P. Michaleris, Thermomechanical model development and in situ experimental validation of the Laser Powder-Bed Fusion Process, Addit. Manuf. (2017), S2214860417300441.
- [23] E.R. Denlinger, V. Jagdale, G. Srinivasan, T. El-Wardany, P. Michaleris, Thermal modeling of Inconel 718 processed with Powder Bed Fusion and experimental validation using in situ measurements, Addit. Manuf. (2016), S2214860416300380.
- [24] N. Farahi, S. Prabhudev, G.A. Botton, J.R. Salvador, H. Kleinke, Nano- and microstructure engineering: an effective method for creating high efficiency magnesium silicide based thermoelectrics, ACS Appl. Mater. Interfaces (2016) accami 6b12297
- [25] J. Li, J.P. Longtin, S. Tankiewicz, A. Gouldstone, S. Sampath, Interdigital capacitive strain gauges fabricated by direct-write thermal spray and ultrafast laser micromachining, Sens. Actuators A Phys. 133 (1) (2007) 1–8.
- [26] Z. Bo, Z. Lei, G. Fu, X. Shi, S. Sampath, Thermoelectric properties of magnesium silicide prepared by thermal spraying, ASME 2012 Heat Transfer Summer Conference collocated with the ASME 2012 Fluids Engineering Division Summer Meeting and the ASME 2012 10th International Conference on Nanochannels, Microchannels, and Minichannels, 2012.
- [27] H. Zhang, T. Zheng, B. Gnade, K. Cho, The effect of point defects and nanoparticles on thermal conductivity of magnesium silicide, Comput. Mater. Sci. 104 (2015) 172–176.
- [28] K. Sharifian, M. Emamy, K. Tavighi, S.E. Vaziri Yeganeh, Microstructures and tensile properties of hot-extruded Al matrix composites containing different amounts of Al4Sr, Metall. Mater. Transf. A 45 (12) (2014) 5344–5350.
- [29] Q.D. Qin, Y.G. Zhao, W. Zhou, P.J. Cong, Effect of phosphorus on microstructure and growth manner of primary Mg2Si crystal in Mg2Si/Al composite, Mater. Sci. Eng. A 447 (1–2) (2007) 186–191.
- [30] C. Li, Y.Y. Wu, H. Li, X.F. Liu, Morphological evolution and growth mechanism of primary Mg2Si phase in Al-Mg2Si alloys, Acta Mater. 59 (3) (2011) 1058–1067.
- [31] G.R. Hadley, Thermal-conductivity of packed metal powders, Int J. Heat. Mass Transf. 29 (6) (1986) 909–920.
- [32] S. Kou, Y. Wang, Weld pool convection and its effect, Weld. J. 65 (3) (1986) 63s–70s.
- [33] S. Patankar. Numerical Heat Transfer and Fluid Flow, CRC Press, 1980.

- [34] B. Van Leer, Towards the ultimate conservative difference scheme. II. Monotonicity and conservation combined in a second-order scheme, J. Comput. Phys. 14 (4) (1974) 361–370.
- [35] H.K. Versteeg, W. Malalasekera. An Introduction to Computational Fluid Dynamics: The Finite Volume Method, Pearson Education, 2007.
- [36] W. Tao. Numerical Heat Transfer, Second ed., Xi'an Jiaotong University Press, 2001.
- [37] M. Akasaka, T. Iida, A. Matsumoto, K. Yamanaka, Y. Takanashi, T. Imai, N. Hamada, The thermoelectric properties of bulk crystalline n- and p-type Mg2Si prepared by the vertical Bridgman method, J. Appl. Phys. 104 (1) (2008).
- [38] B.H. Yu, D. Chen, Q.B. Tang, C.L. Wang, D.H. Shi, Structural, electronic, elastic and thermal properties of Mg2Si, J. Phys. Chem. Solids 71 (5) (2010) 758–763.
- [39] C. Glassbrenner, G.A. Slack, Thermal conductivity of silicon and germanium from 3 K to the melting point, Phys. Rev. 134 (4A) (1964) A1058.
- [40] G. Chen. Nanoscale Energy Transport and Conversion: A Parallel Treatment of Electrons, Molecules, Phonons, and Photons, Oxford University Press, Oxford; New York, 2005.
- [41] S. Kou, Y. Wang, Three-dimensional convection in laser melted pools, Metall. Trans. A 17 (12) (1986) 2265–2270.